JLT-34410-2024

Single-mode Sapphire Fiber Temperature Sensor

Mohan Wang, Patrick S. Salter, Frank P. Payne, Adrian Shipley, Igor N. Dyson, Tongyu Liu, Tao Wang, Kaihui Zhang, Jian Zhang, Zhitai Jia, Stephen M. Morris, Martin J. Booth, and Julian A. J. Fells

***Abstract*— Sapphire fiber can withstand temperatures of around 2000°C, but it is multimoded, giving poor precision sensors. We have demonstrated a single-mode sapphire fiber Bragg grating temperature sensor operating up to 1200°C. A single-mode sapphire fiber was formed by writing a depressed cladding waveguide along the length of a 100-µm diameter sapphire fiber using a femtosecond laser. A second-order Bragg grating sensor was inscribed within the waveguide, achieving a reflectivity of >90% and a narrow bandwidth of <0.5 nm. The single-mode sapphire fiber was fusion spliced to standard silica single-mode fiber. The sensor was vibration-tested over a 10 Hz to 30 kHz range with 30 µm displacement, resulting in minimal Bragg wavelength variation of <30 pm standard deviation. The sensor was furnace-tested to 1200°C, showing ±0.08% repeatability above 1000°C. This demonstrates the high precision sensing capability of single-mode sapphire fiber Bragg grating sensors with end-to-end single mode interrogation.**

***Index Terms*—Fiber Bragg gratings, Optical fiber sensors, Laser materials processing**

I. Introduction

OPTICAL fiber sensors are commonly used for remotely monitoring a wide range of infrastructure and machinery. High-quality monitoring of environmental parameter changes can improve safety, extend lifetime, lower environmental impact, and prevent potential failures at an early stage. However, there are many applications, particularly in the energy, aerospace and space sectors, where operating temperatures are beyond the 1000°C limit of silica fiber sensors [1].

An important class of sensor is the fiber Bragg grating (FBG), which is a periodic modification of the effective refractive index along the length of an optical fiber. An FBG reflects light predominantly at a wavelength determined by the product of the effective refractive index and the physical period. As these properties are temperature dependent, FBGs can operate as temperature sensors. However, as temperatures approach 1000°C, there is considerable drift in the wavelength of reflection in silica fibers over time [1]. Although pre-annealed silica fiber can withstand 1200°C for up to 20 hours [2], the peak reflectivity degrades over time. The mechanical strength of silica fiber also decreases at temperatures above the softening temperature of 1050°C, making it unsuitable for many applications.

As an alternative, sapphire optical fiber can withstand far higher temperatures up to 2000°C. Multimode sapphire FBGs have been fabricated using a phase-mask [3], [4], with interferometric [5], and with parallel dotted lines [6]. These sensors have been demonstrated up to 1900°C [7], [8], with long-term stability tests up to 1400°C for 28 days [9], and under 1000°C for 48 days [10]. Sapphire fiber is a high refractive index single-crystal without a cladding, and therefore highly multimoded. Since different modes have different effective refractive indices, Bragg gratings in sapphire fiber typically have a very broad reflection spectrum [11]. Furthermore, the power distribution between the modes changes with environmental factors such as temperature and vibration. This severely compromises the measurement precision attainable and reduces the number of sensors which may be multiplexed.

There have been attempts to create a cladding around a sapphire fiber by adding additional coatings [12] or wrapping it around silica [13]. However, a cladding material that can match the operating temperature of sapphire has not been identified. Other approaches include creating an inner cladding within the fiber by irradiation [14], reducing the core diameter by etching in hot acid [15], [16], [17], or using a photonic crystal-like design [18]. However, in all these cases, the resulting fiber was still multimode. There have been numerical studies on making higher-order modes in sapphire fiber lossy by having holes in the side of the fiber [19], but these devices have not been realized experimentally.

It is possible to launch into the fundamental mode of multimode sapphire fiber by optimizing the launch conditions [20], [21], using a tapered single-mode fiber [22], or bending the sapphire FBG [23]. However, although it may be possible to launch into a particular mode of multimode fiber, coupling to other modes will occur and vary with environmental conditions [24], causing fluctuations in the spectra and inaccuracies in sensing.

We previously demonstrated a 1 cm single-mode sapphire FBG written on a 425 µm diameter sapphire fiber with 2 dB/cm propagation loss, fabricated using femtosecond laser direct writing [25]. However, it was not possible to fusion

This work was supported by the Engineering and Physical Sciences Research Council (EP/T00326X/1). (Corresponding author: Julian A. J. Fells).

Mohan Wang, Patrick S. Salter, Frank P. Payne, Igor N. Dyson, Tongyu Liu, Stephen M. Morris, Martin J. Booth, and Julian A. J. Fells are with the Department of Engineering Science, University of Oxford, Parks Road, Oxford, OX1 3PJ, UK (e-mail: mohan.wang@eng.ox.ac.uk, julian.fells@eng.ox.ac.uk).

Adrian Shipley is with the Rolls-Royce Plc, Derwent Building, 5000 Solihull Parkway, Birmingham Business Park, Birmingham, B37 7YP, UK.

Tao Wang, Kaihui Zhang, Jian Zhang, Zhitai Jia are with the State Key Laboratory of Crystal Materials, Shandong University, 27 South Shanda Road, Jinan, Shandong, 250100, China (email: jia.zhang@sdu.edu.cn, z.jia@sdu.edu.cn).

Tao Wang is also with the Jiangsu Jingying Optoelectronics Technology Co. LTD, 10 East Zhujiang Road, Xuzhou, Jiangsu, 221116, China (email: t.wang@sdu.edu.cn).

splice the 425-µm sapphire fiber to a standard single-mode silica fiber, and longer devices are required for sensing. Recently, we demonstrated on planar sapphire substrates that the propagation loss can be optimized to be as low as 0.8 dB/cm by adding layers to the depressed cladding waveguide and carefully designing the geometry [26]. However, it is significantly harder to reproduce this result on a sapphire fiber. Sapphire fibers typically have an inhomogeneous cross-section along their fiber length [12], while the smaller fiber diameter makes it more susceptible to cracking. Furthermore, extensive correction is required for the rounded hexagonal fiber surface [27]. In this paper we use an improved design and writing process to extend the length of the single-mode sapphire fiber and improve the spectral performance of the Bragg grating. A single-mode sapphire FBG sensor has been spliced to a single-mode silica fiber and tested as a high-precision temperature sensor at ultrahigh temperatures.

II. Design and Fabrication

As femtosecond laser exposure results in a reduction in the sapphire refractive index, the waveguide used is a depressed cladding waveguide [28]. The waveguide is formed by leaving the core unmodified and laser-writing the material around the core to reduce its refractive index, thereby forming the cladding. A diagram of a depressed cladding waveguide is shown in Fig. 1(a). It consists of three regions: a core area with a refractive index of n_1, a cladding with a slightly lower refractive index of n_2, and an outer cladding which has the same refractive index as the core, n_1. The dominant loss in a depressed cladding waveguide is the radiative loss [29], which is dependent on the cladding-to-core radius ratio according to Eq. 8 in Ref. [29]. Since in our case the outer cladding refractive index is the same as the core index, all modes are leaky [29]. However, the theoretical loss is reduced dramatically with increasing cladding-to-core ratio.

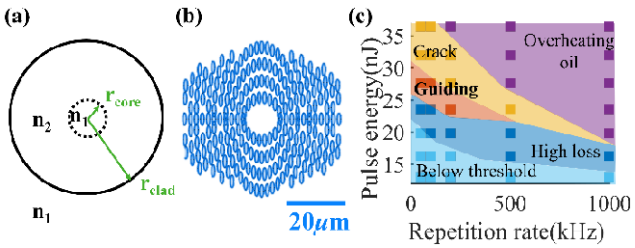


Fig. 1. (a) Diagram of a depressed cladding waveguide, (b) single-mode waveguide design layout with a cladding-to-core ratio of 5; each ellipse represents a line of laser-modified index change along the fiber length, and (c) the fabrication parameter window, showing the influence of laser pulse energy and repetition rate on the waveguide design in (b). The fabrication parameters for the waveguide were chosen from the area labeled 'Guiding'.

A multilayer depressed cladding single-mode waveguide was designed based on a refinement of our previous work [25], [26]. The design is shown Fig. 1(b) and has a core radius of 5 µm, with tracks around it to form the cladding. Each track, is a straight line of laser modification along the fiber, formed by translating the fiber against the fixed laser focus. The tracks are represented in Fig. 1(b) as ellipses due to the asymmetry in the laser focus and resulting refractive index modification. The height and width of the tracks are 4 and 1.2 µm respectively, as measured experimentally.

The depressed cladding has a radius of 25 µm, with additional tracks added to the left and right sides to make the cladding more circular [30], [31]. With a cladding-to-core ratio of 5, the theoretical propagation loss is expected to be <0.5 dB/cm [25]. The geometry was carefully arranged to fill the designed shape with laser-written tracks using the measured dimensions. The neighboring tracks were as close to one another as possible, while avoiding cracking. The spacings between the tracks were set to be >5.5 and >1.5 µm in the vertical and horizontal directions, respectively. Due to laser power fluctuation the actual track size can vary slightly, so the intervals are adjusted before each fabrication to maintain consistency. The design consists of between 200 to 250 tracks.

The fibers were fabricated using a custom laser-heated pedestal growth system [32], [33]. The *C*-axis was along the fiber length. The fiber was processed using a regenerative femtosecond laser system (Pharos SP-06-1000-PP) delivering 170 fs pulses at 515 nm. The output beam was expanded using a telescope and projected onto a spatial light modulator (SLM). A pre-distorted phase pattern was applied to the SLM to correct for aberrations inside the laser beam delivery system. The pre-distorted beam was projected onto the pupil plane of the objective through a 4-*f* imaging telescope. The linearly polarized laser beam was focused onto the fiber through a ×63 1.25 NA oil objective through immersion oil (Cargille Labs, n = 1.7450).

The structure was fabricated using a three-step process. First, the bottom layers of the depressed cladding were written using a pulse energy of 26 - 28 nJ and 2 - 4 mm/s writing speed at a repetition rate of 50 - 100 kHz. This writing speed range was found to be the maximum possible speed to keep the index matching oil stable under the objective, without being disturbed by the fiber movement. Figure 1(c) shows the influence of repetition rate and pulse energy on writing the design in Fig. 1(b), when using a speed of 2 mm/s. A higher repetition rate and pulse energy would be desirable, to increase the refractive index contrast between the laser-written cladding and the unmodified core, leading to a higher normalized frequency and lower loss. However, the 100-µm diameter sapphire fiber is very susceptible to cracking. Only a narrow fabrication window was found between a refractive index contrast that is too small to support guiding, and overheating the oil or generating cracks during fabrication, as shown in in Fig. 1(c).

The Bragg grating was then inscribed within the center of the waveguide, close to one end of the fiber, using a pulse energy of 30 - 40 nJ and a speed of 0.1 - 2 mm/s. A second order grating was chosen for optimum refractive index modulation. The period was calculated using the refractive index of sapphire at 1550 nm (n = 1.74628) to be 887.64 nm. The grating was written using modulated bursts, enabled by

the pulse synchronization output (PSO) of the Aerotech stage. The laser output was further windowed into a burst train with a repetition rate of $f_{rep} = v/\Lambda$, where v is the writing speed and Λ is the period of the grating. The number of pulses per period could be controlled by adjusting the duty cycle of the PSO function. Finally, the top layers of the waveguide were written (with the same parameters as the bottom layers) to enclose the grating. It took 1-2 hours to fabricate a 4-cm FBG. A detailed investigation of the optimum fabrication parameters for waveguide Bragg gratings can be found in [26].

After fabrication, the fiber was polished on both ends down to 0.1 micrometer grit following the Thorlabs polishing guidebook (Thorlabs FN96A). Figures 2(a) and 2(b) show the end-facet views of the FBG from the waveguide end and the grating end, respectively. Cracks can be seen in Fig. 2(a) and 2(b), which were incurred by stress introduced during polishing and are confined to within close proximity of the fiber end facets. The top view of the grating is shown in Fig. 3. The leftmost image shows the waveguide and grating in the center of the fiber. The images are in increasing magnification from left to right. In the rightmost image, the boundaries of the core and cladding regions can be seen, with the grating lines clearly visible in the center of the core.

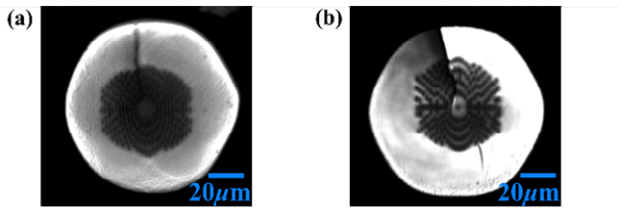


Fig. 2. Images of the waveguide end facet (a) and grating end facet (b) written on a 100-μm diameter sapphire fiber.

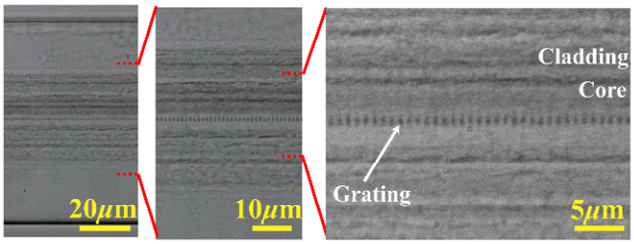


Fig. 3. Top view of the waveguide and grating written on a 100-μm diameter sapphire fiber. The magnification increases from left to right. The waveguide is based on the design in Fig. 1(b), fabricated using 28 nJ pulse energy, 100 kHz repetition rate, and 2 mm/s writing speed. The grating is second-order with a period of 887.64 nm, fabricated using modulated bursts inside the cladding with 35 nJ pulse energy and 22 pulses per period.

Through tuning the waveguide design and fabrication conditions, no cracks were observed in or around the Bragg grating and waveguide region along the 4 cm sensor, as shown in Fig. 3, except for around the facets. Similar observations of crack formation during polishing have been reported in depressed cladding waveguides written inside Nd:YAG crystal [34]. By virtually eliminating the cracking, as compared to our previous work [25], we have greatly improved the sensor's mechanical stability. As the cracks on the end facets do not impact the waveguide core, they have minimal impact on the FBG performance.

III. Characterization

A tunable laser (Agilent 8164A) was coupled to a silica single-mode fiber (SMF, SMF28e+ equivalent) with a cleaved end. This was butt-coupled to a single-mode sapphire fiber to measure the mode profile. The near-field mode-field profile was recorded on an InGaAs camera (Hamamatsu C14041-10U) using an imaging system. The mode profile at 1550 nm from a 4-cm long sapphire FBG is shown in Fig. 4(a). The sapphire fiber has a single-mode waveguide along its entire length.

There is a 1 cm long second order Bragg grating at one end of the fiber within the core. The waveguide was written at a sample translation speed of 2 mm/s with a repetition rate of 100 kHz and a pulse energy of 28 nJ. The grating was written at a speed of 0.1 mm/s and a pulse energy of 35 nJ, with a duty cycle of 1%, and 22 pulses per period. The mode field diameter (MFD) was calculated from a Gaussian fit to obtain the full width at $1/e^2$ intensity. The MFD is 11.4 and 11.3 μm in the horizontal and vertical directions respectively, which yields a theoretical mode mismatch loss of ~ 0.03 dB when coupled to SMF28e+. A refractive index modification of $\Delta n = -3.0 \times 10^{-3}$ was calculated by solving the Helmholtz equation for a step index fiber [25]. The corresponding normalized frequency is $V = 2.11$, which is below the cut-off value of 2.405, indicating that the waveguide is single-mode.

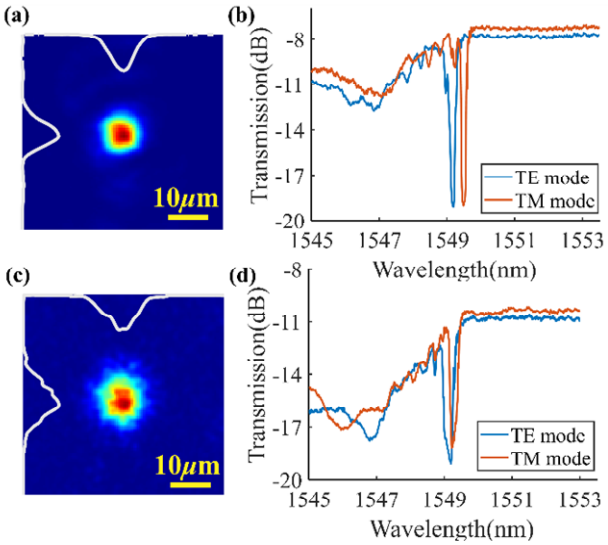


Fig. 4. (a) Transmission mode field of a 4-cm long single-mode FBG, with mixed polarized input light at 1550 nm, measured at the single-mode waveguide side, (b) the transmission spectra of the same 4-cm FBG for the two orthogonal polarizations, measured using a swept tunable laser and photodetector setup, and (c-d) the transmission mode field (c) and the transmission spectra (d) of the same FBG after being annealed at 1200°C. See Dataset 1 for the underlying data.

The transmission spectrum was measured by replacing the camera with a power meter (Newport 1919-R with 818-IG detector), and by calculating the power difference between the transmitted power with and without the sapphire fiber. A manual polarization controller was used to adjust the laser polarization. Fig. 4(b) shows transmission spectra, measured at a resolution of 10 pm for both the transverse electric (TE) and transverse magnetic (TM) polarizations. The corresponding Bragg wavelengths were measured to be 1549.20 and 1549.49 nm, respectively. The origin of the birefringence is likely due to the anisotropic refractive index distribution of the grating, as each track is elliptical in shape. This could potentially be solved by using a line-by-line or plane-by-plane inscription of the grating [35].

The modulated bursts enabled flexibility in tuning the grating properties, such as the refractive index perturbation, allowing a higher reflectivity to be achieved. The difference in transmission at the Bragg wavelength and at 1550 nm was measured to be 11.4 and 11.7 dB, for the respective polarizations, indicating reflectivities of 92.7% and 93.3%. The 3-dB bandwidths were measured to be 0.12 and 0.14 nm, respectively. The propagation loss of the single-mode waveguide was measured using a cut-back method to be ~ 1.5 dB/cm for both polarizations. This number is higher than the theoretical estimation, which is likely due to additional scattering loss caused by an inhomogeneous refractive index distribution [36]. The propagation loss is larger than that demonstrated in our previous work on a sapphire bulk because of the smaller index contrast between the laser-written cladding and the sapphire core [26]. As can be seen from Fig. 1(c), a lower pulse energy and a lower repetition rate were chosen to mitigate cracking and bubble generation, owing to the small size of the sapphire fiber.

The FBG was placed inside a box furnace for annealing. The temperature was raised from room temperature to 1200°C over seven hours, held at 1200°C for one hour, and then dropped to room temperature at the natural cooling rate. The mode profile after annealing is shown in Fig. 4(c). The MFD is 14.1 and 16.5 μm in the horizontal and vertical directions, respectively, suggesting a halving in the cladding refractive index modification to $\Delta n \approx -1.5 \times 10^{-3}$. The normalized frequency was reduced to $V = 1.41$, well below the single-mode cut-off. Figure 4(d) shows the transmission spectra of both polarizations, with the Bragg peaks for the TE and TM polarizations measured to be 1549.15 and 1549.27 nm, and the 3-dB bandwidths to be 0.27 and 0.23 nm, respectively. The reflectivity was calculated from the transmission dip to be 84.8% and 82.4% for the respective polarizations. The annealing has lowered the birefringence of the waveguide, reducing the wavelength separation between polarization modes from 290 pm to 120 pm. In both Figs. 4(b) and 4(d) there is loss at shorter wavelengths, likely due to coupling to cladding modes as is also observed in silica FBGs. However, by positioning cascaded FBGs in order of increasing wavelength, the transmission loss at the short wavelength side would not impact sensor performance.

IV. Sensor Splicing

A 4-cm single-mode fiber sensor with a silica fiber tail was prepared for high-temperature testing, as schematically illustrated in Fig. 5. The sapphire fiber end furthest from the grating was spliced to standard silica SMF using a fusion splicer (Sumitomo Type-72C) in manual mode. There have been many successful reports of splicing multimode sapphire fibers to conventional or tapered silica fibers [6], [11], [14], [22], [37], [38]. However, splicing the single-mode sapphire fiber to silica SMF is much more difficult due to the need for matched mode fields and precise core alignment.

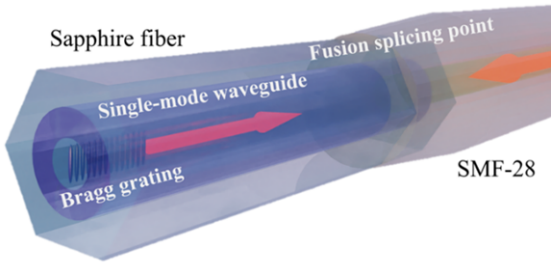


Fig. 5. Schematic of the sapphire sensor.

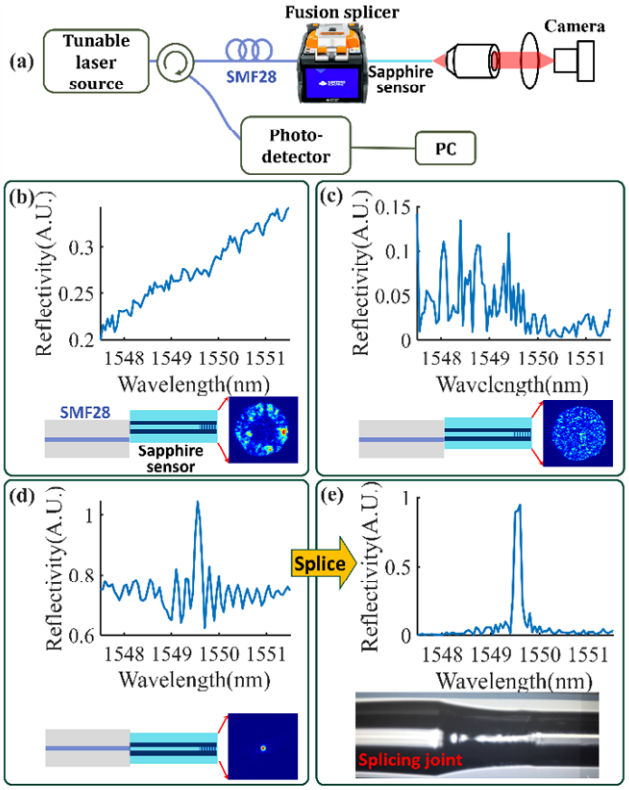


Fig. 6. (a) Schematic of the sensor fusion splicing setup. (b-d) Example reflection spectra (top) and schematics of the relative position (bottom) during one iterative manual fiber adjustment process. Light from the single-mode silica fiber was coupled: (b) between the cladding and sapphire surface, (c) into the depressed cladding, and (d) into the single-mode sapphire waveguide core. (e) the spectrum after a successful splice from the optimized position (top), and the image of the splicing joint after a successful splice (bottom).

The first challenge is that the waveguide is not perfectly located at the core of the sapphire fiber due to the asymmetric hexagonal shape of the sapphire fiber. As splicer imaging systems do not have aberration compensation for the high index sapphire, it is not possible to use visual core alignment. The second challenge is that the splicing parameters need to be carefully controlled to avoid excessive damage to the laser written waveguide and avoid movement of the fibers during the splicing. Unlike multimode fiber, even relatively small displacements between the single-mode fiber core and the single-mode sapphire can result in unusable devices.

Using the splicer positioning stages, precise core alignment was achieved through an iterative manual fiber adjustment process, using the setup in Fig. 6(a). The Bragg reflection spectrum was monitored using the reflection measurement setup to inject light into the grating via the silica SMF. The same tunable laser (Agilent 8164A) was coupled to an optical circulator to inject light into the grating, with the reflected light monitored on a photodetector within the 8164A. Figures 6(b-d) show spectra recorded at different stages during an example splice, taken at a coarse resolution of 50 pm and a bandwidth of 4 nm for better time efficiency. They also show schematics of the relative position between the sapphire sensor and silica fiber. An imaging system was used to view the end facet of the sapphire fiber emerging from the splicer.

With light butt-coupled between the depressed cladding waveguide and the sapphire fiber surface, random reflected light from the sapphire fiber surface and the end facet gives a broadband reflection spectrum [Fig. 6(b)]. As the core of the silica-core fiber is moved closer to the depressed cladding, fluctuations at the shorter wavelength side started to appear [Fig. 6(c)]. When the cores of the single-mode silica and sapphire fibers became aligned, a single Bragg resonance peak is clearly visible [Fig. 6(d)]. Fine tuning of the fiber position is used to maximize the magnitude of the reflected light at the Bragg wavelength. Once an optimum fiber alignment was obtained, the arc fusion process was initiated.

The splicing was performed with both fibers positioned to the center. The melting temperature of sapphire is much higher than the softening temperature of silica. During the splicing and when heated by the arc, the silica fiber first softens. As sapphire has a higher coefficient of thermal expansion (CTE), (CTE = ~ 8×10^{-6}) than silica (CTE = 0.5×10^{-6}), the sapphire fiber expands to touch the melted silica fiber. A 'cap' is formed with silica bonded to the sapphire fiber. The process has been well-studied in crystalline fibers [39]. Figure 6(e) shows the reflection spectrum and an image of the splice joint (taken using the splicer built-in camera) for a successful splice.

We used an arc time of 2 seconds and a pre-fuse time of 0.15 seconds, with a normal pre-fuse and a reduced fuse current, to protect the laser-written sapphire fiber cladding from excess heating. These splicing parameters were optimized following detailed guidance described in [40] for optimizing sapphire-silica arc fusion splicing. The spliced sensor was very robust during moving and testing. No extra protection was applied to protect the splicing point. Full details of the splicer parameters, together with example images of splices are included in the Supplementary Information.

V. High Temperature Testing

The sapphire fiber sensor with its lead-in silica SMF tail was inserted through a ceramic tube opening into a box furnace with a maximum temperature of 1200°C. A Type-K thermocouple was placed in proximity to the sensor. Temperature cycling tests were then performed over a period of 9 days. The sensor was first taken to 1000°C and back down to room temperature. The sensor was then taken through six repeated heating and cooling cycles (Cycles 1-6) in 100°C steps up to 1200°C. The temperature was held at 1200°C for 1 hour during Cycle 1 for annealing. We expected the sensor to require annealing at a temperature above 1200°C for operation at 1200°C [8]. However, the above-mentioned annealing conditions worked fine for our repeatability test, with negligible hysteresis and minimal drifting between cycles.

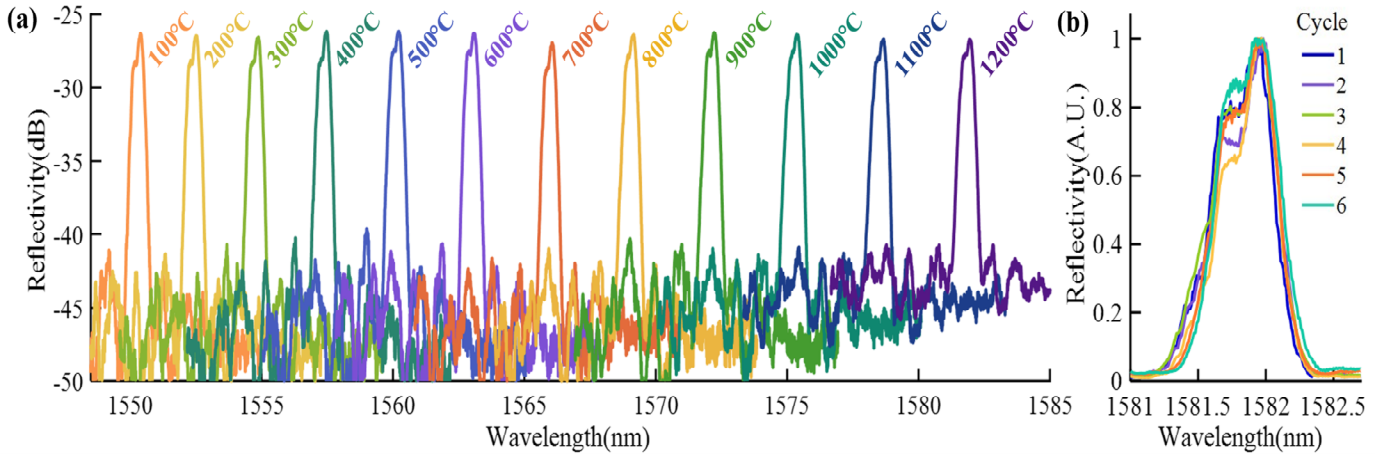


Fig. 7. (a) Spectra of the sapphire FBG during the fifth heating cycle, with spectra at each temperature step of 100°C overlaid, and (b) spectra at 1200°C for all six heating cycles. The magnitude was normalized. See Dataset 1 for the underlying data.

Future work is required to identify the optimal annealing condition for the single-mode sapphire sensor for long term operation and higher temperatures.

Reflection spectra were measured using the same tunable laser and photodetector setup as described in Part II. At each temperature, the reflection spectrum was measured over a 10 nm range with a 10 pm step size. Figure 7(a) shows spectra at each temperature overlaid for Cycle 5. There is an increase in the noise background as the temperature increases, but the signal-to-noise ratio (SNR) remains over 16 dB across the full range.

Figure 7(b) shows the overlaid spectra at a temperature of 1200°C for all cycles, showing a consistent peak wavelength. The asymmetrical shape of the reflection peak is due to the existence of two polarizations in the injection light. A manual polarization controller was added to the setup, and the input polarization was adjusted to reveal two orthogonal polarization modes. Two peaks were observed which had a separation of 0.43 nm. However, commercial interrogators typically have a polarization scrambler. As the modes are distinct, it would be possible to determine the wavelength of both peaks with a scrambled input polarization and take a mean value.

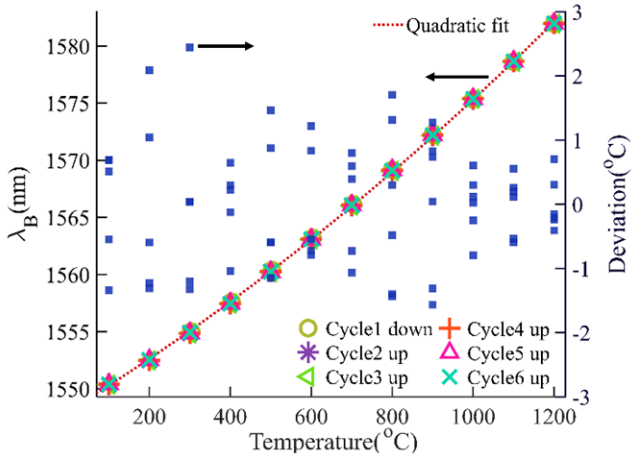


Fig. 8. Left axis: Bragg wavelength against temperature for six heating and cooling cycles, with a quadratic fit calibration curve. Right axis: Temperature measurement deviation from the mean reading using the calibration curve. See Dataset 1 for the underlying data.

Figure 8 shows the Bragg wavelength against temperature, for Cycles 1-6. The Bragg wavelength was determined by extracting the maximum value from interpolated spectra. We used a quadratic fit $\lambda_B = A + BT + CT^2$, with A, B, and C found to be 1548.09 nm, 21.60 pm/°C, and 0.0056 pm/°C^2 respectively, which are consistent with the literature [38]. The sensitivity varies between 22.7 to 35.1 pm/°C. Also shown in Fig. 8 is the residual temperature deviation at each temperature point, obtained by subtracting the mean Bragg wavelength and dividing it by the gradient of the characteristic curve at that point. The variation was within ±2.5°C. Much of this variation is likely due to the furnace temperature varying over the 15-minute time interval it took to take each spectrum. The furnace did not have cooling, hence the control system had much better stability at higher temperatures. There is also the ±0.5°C accuracy of the thermocouple to consider. However, above 1000°C, the variation is within ±0.8°C, or within ±0.08%, which is significantly better than previous measurements [11]. The fiber length is around that needed to access a gas turbine and the high SNR gives potential to increase the length.

VI. Vibration Testing

The sensor probe will be subject to vibration in many real-world environments, for example gas turbines. In order to test the vibration sensitivity, a spliced FBG sensor was attached to the diaphragm of a loudspeaker. A function generator was used to induce vibration at a set of frequencies from 10 Hz to 3 kHz, which roughly covers the vibration frequency range of a turbine blade under normal operation [41]. The displacement at 10 Hz was measured to be 30 µm with the assistance of an imaging system.

A commercial interrogator (SmartFibres) was used to acquire the spectrum at a sampling frequency of 2.5 Hz and a wavelength resolution of 10 pm. Although technically this is below Nyquist sampling, in practice the vibration disturbance is likely to result in random fluctuation between sampling points. At each frequency, 1000 spectra were collected, and the Bragg wavelengths were extracted using a spline fit.

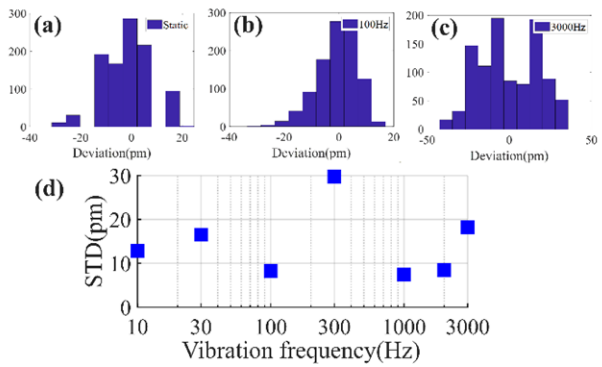


Fig. 9. (a-c) The histograms of the Bragg wavelength deviation for no vibration (a), at a vibration frequency of 100 Hz, (b) at a vibration frequency of 3000 Hz (c), and (d) the standard deviation of Bragg wavelength drift at vibration frequencies of between 10 to 3000 Hz. See Dataset 1 for the underlying data.

Figure 9 shows the histogram of the measured Bragg wavelengths when the sensor was: (a) static, (b) under vibration at 100 Hz, and (c) under vibration at 3000 Hz. The standard deviation (STD) across the measured frequency range is summarized in Fig. 9(d). The STD under static conditions was 9.10 pm. The maximum STD was less than 30 pm at 300 Hz, which corresponds to a temperature STD of 1.3°C. This is comparable to the fluctuation observed at low temperatures, noting that the thermocouple has an accuracy of ±0.5°C.

VII. Discussion

Sapphire can survive far higher temperatures than 1200°C, potentially up to 2000°C. The current test temperature was limited not only by the available furnace, but also by the sapphire fiber length. Extending the sapphire fiber length would enable the splice point to be further away from the high temperature measurement location. This in turn would allow higher measurement temperatures, whilst keeping the splice point at a temperature where degradation does not occur. Some applications may also have better insulation casings allowing higher temperature gradients, thereby enabling the splice point to be kept within its safe operating range while sensing higher temperatures.

The current length of the sapphire fiber is well within the travel range of the translation stages, and longer stages are readily available. The maximum length of the sapphire fiber achievable is currently limited by the waveguide loss. Further work is required to lower the current propagation loss of 1.5 dB/cm, which could potentially be achieved by increasing the waveguide refractive index contrast or by adopting a more optimized geometry.

The modulated burst method enables better control of the FBG performance than the ring-by-ring writing demonstrated in our previous work [25]. As the coupling coefficient and the refractive index perturbation can be easily tuned by adjusting the duty cycle and the numbers of pulses per period, optimization of the reflectivity is achieved. A drawback of the modulated burst method is the birefringence of the grating, which can potentially be solved by line-by-line scanning for a symmetric FBG modification at the cross-section. Further multiplexing is also possible by decreasing the length of each grating and increasing the length of the single-mode sapphire waveguide.

VIII. Conclusion

We fabricated a single-mode sapphire fiber Bragg grating temperature sensor with a standard single-mode silica fiber tail, using femtosecond laser direct writing and arc fusion splicing. The FBG has a reflectivity of >90% with a -3 dB bandwidth of <0.5 nm. The SNR was measured to be >16 dB across the operational temperature range. A 4-cm long sapphire sensor probe with a 1-cm FBG at its tip was tested in a furnace up to 1200°C, showing a sensitivity between 22.7 to 35.1 pm/°C. The repeatability above 1000°C was within ±0.08%. Vibration testing over a frequency range of 10 Hz to 3 kHz with 30 μm displacement showed the Bragg wavelength to vary with a STD of <30 pm. This equates to a temperature STD of <1.3°C. The single-mode sapphire sensor provides an alternative to existing multimode sapphire sensor technologies and without the need of extra cladding, external packaging, or a complicated demodulation system. The work shows the potential for single-mode sapphire fiber sensors for ultra-extreme environments, such as applications in energy, space, and aerospace.

Data Availability

The underlaying data for Figs. 4, 7, 8 and 9 are provided in Dataset 1 of the Supplementary Information [42]. The Supplementary Information also has a document with guidance for splicing single-mode sapphire fiber to silica fiber, the splicer parameters, and images of good and poor splices. For the purposes of open access, the authors have applied a Creative Commons Attribution (CC-BY) license to any Author Accepted Manuscript version.

Acknowledgment

The authors gratefully acknowledge the support and advice of their partners Rolls-Royce plc., Cranfield University, UK Atomic Energy Authority and MDA Space and Robotics. The authors thank Prof Felix Hofmann and Miss Diana Passmore for the use of the furnace. They thank Professor Dominic O'Brien, Dr Fabian Pokorny, Dr Richard Reeves, and Dr Stuart Higgs for the use of equipment. They also thank the anonymous Reviewers who have helped to significantly improve this manuscript.

References

[1] D. Grobnic, C. Hnatovsky, S. Dedyulin, R. B. Walker, H. Ding, and S. J. Mihailov, "Fiber bragg grating wavelength drift in long-term high temperature annealing," *Sensors*, vol. 21, no. 4, pp. 1–29, 2021, doi: 10.3390/s21041454.

[2] Y. Li *et al.*, "Fiber Bragg gratings with enhanced thermal stability by residual stress relaxation," *Optics Express, Vol. 17, Issue 22, pp. 19785-19790*, vol. 17, no. 22, pp. 19785–19790, Oct. 2009, doi: 10.1364/OE.17.019785.

[3] D. Grobnic, S. J. Mihailov, C. W. Smelser, and H. Ding, "Sapphire fiber bragg grating sensor made using femtosecond laser radiation for ultrahigh temperature applications," *IEEE Photonics Technology Letters*, vol. 16, no. 11, pp. 2505–2507, Nov. 2004, doi: 10.1109/LPT.2004.834920.

[4] M. Busch, W. Ecke, I. Latka, D. Fischer, R. Willsch, and H. Bartelt, "Inscription and characterization of Bragg gratings in single-crystal sapphire optical fibres for high-temperature sensor applications," *Meas Sci Technol*, vol. 20, no. 11, 2009, doi: 10.1088/0957-0233/20/11/115301.

[5] T. Elsmann, T. Habisreuther, A. Graf, M. Rothhardt, and H. Bartelt, "Inscription of first-order sapphire Bragg gratings using 400 nm femtosecond laser radiation," *Opt Express*, vol. 21, no. 4, p. 4591, Feb. 2013, doi: 10.1364/OE.21.004591.

[6] G. Shi, R. Shurtz, G. Pickrell, A. Wang, and Y. Zhu, "Point-by-point inscribed sapphire parallel fiber Bragg gratings in a fully multimode system for multiplexed high-temperature sensing," *Opt Lett*, vol. 47, no. 18, p. 4724, Sep. 2022, doi: 10.1364/OL.471370.

[7] T. Habisreuther, T. Elsmann, Z. Pan, A. Graf, R. Willsch, and M. A. Schmidt, "Sapphire fiber Bragg gratings for high temperature and dynamic temperature diagnostics," *Appl Therm Eng*, vol. 91, pp. 860–865, 2015, doi: 10.1016/j.applthermaleng.2015.08.096.

[8] T. Elsmann, T. Habisreuther, A. Graf, M. Rothhardt, M. A. Schmidt, and H. Bartelt, "1.2.4 - First-order sapphire fiber Bragg gratings for high temperature sensing," *Tagungsband*, pp. 53–58, May 2016, doi: 10.5162/SENSOREN2016/1.2.4.

[9] T. Habisreuther *et al.*, "Long-term stable sapphire fiber Bragg grating sensors at 1400°C," *23rd International Conference on Optical Fibre Sensors*, vol. 9157, no. June 2014, p. 915719, 2014, doi: 10.1117/12.2059313.

[10] S. Yang *et al.*, "Application of sapphire-fiber-bragg-grating-based multi-point temperature sensor in boilers at a commercial power plant," *Sensors (Switzerland)*, vol. 19, no. 14, pp. 1–13, 2019, doi: 10.3390/s19143211.

[11] B. Wang, Y. Niu, X. Qin, Y. Yin, and M. Ding, "Review of high temperature measurement technology based on sapphire optical fiber," *Measurement (Lond)*, vol. 184, Nov. 2021, doi: 10.1016/J.MEASUREMENT.2021.109868.

[12] H. Chen, M. Buric, P. R. Ohodnicki, J. Nakano, B. Liu, and B. T. Chorpening, "Review and perspective: Sapphire optical fiber cladding development for harsh environment sensing," *Appl Phys Rev*, vol. 5, no. 1, Mar. 2018, doi: 10.1063/1.5010184.

[13] Q. Guo *et al.*, "Sapphire-derived fiber bragg gratings for high temperature sensing," *Crystals (Basel)*, vol. 11, no. 8, 2021, doi: 10.3390/cryst11080946.

[14] B. A. Wilson and T. E. Blue, "Creation of an Internal Cladding in Sapphire Optical Fiber Using the 6Li(n, $α$)3H Reaction," *IEEE Sens J*, vol. 17, no. 22, pp. 7433–7439, 2017, doi: 10.1109/JSEN.2017.2756448.

[15] S. Yang, D. Homa, G. Pickrell, and A. Wang, "Fiber Bragg grating fabricated in micro-single-crystal sapphire fiber," *Opt Lett*, vol. 43, no. 1, p. 62, 2018, doi: 10.1364/ol.43.000062.

[16] C. Hill, D. Homa, B. Liu, Z. Yu, A. Wang, and G. Pickrell, "Submicron diameter single crystal sapphire optical fiber," *Mater Lett*, vol. 138, pp. 71–73, Jan. 2015, doi: 10.1016/J.MATLET.2014.09.105.

[17] C. Hill *et al.*, "Single Mode Air-Clad Single Crystal Sapphire Optical Fiber," *Applied Sciences 2017, Vol. 7, Page 473*, vol. 7, no. 5, p. 473, May 2017, doi: 10.3390/APP7050473.

[18] N. Pfeiffenberger, G. Pickrell, K. Kokal, and A. Wang, "Sapphire photonic crystal fibers," *https://doi.org/10.1117/1.3483908*, vol. 49, no. 9, p. 090501, Sep. 2010, doi: 10.1117/1.3483908.

[19] Y. Cheng *et al.*, "Modal reduction in single crystal sapphire optical fiber," *Optical Engineering*, vol. 54, no. 10, p. 107103, Oct. 2015, doi: 10.1117/1.OE.54.10.107103.

[20] J. He, J. He, X. Xu, X. Yin, and Y. Wang, "Single-mode helical sapphire fiber Bragg grating for high-temperature sensing," in *European Workshop on Optical Fibre Sensors (EWOFS 2023)*, M. Wuilpart and C. Caucheteur, Eds., SPIE, May 2023, p. 128. doi: 10.1117/12.2681899.

[21] Q. Bian, H. Zhu, J. Liang, Y. Yu, and P. Yan, "High-Order Mode Suppression in Sapphire Fiber Bragg Gratings Based on Mode Field Matching Fusion Splicing for Single-Mode Demodulation Systems," *IEEE Sens J*, vol. 23, no. 15, pp. 16953–16959, Aug. 2023, doi: 10.1109/JSEN.2023.3289933.

[22] D. Grobnic, S. J. Mihailov, H. Ding, F. Bilodeau, and C. W. Smelser, "Single and low order mode interrogation of a multimode sapphire fibre Bragg grating sensor with tapered fibres," *Meas Sci Technol*, vol. 17, no. 5, pp. 980–984, 2006, doi: 10.1088/0957-0233/17/5/S07.

[23] C. Zhan, J. H. Kim, S. Yin, P. Ruffin, and C. Luo, "High temperature sensing using higher-order-mode rejected sapphire fiber gratings," *Optical Memory and Neural Networks 2007 16:4*, vol. 16, no. 4, pp. 204–210, Dec. 2007, doi: 10.3103/S1060992X07040030.

[24] T. Mizunami, T. V. Djambova, T. Niiho, and S. Gupta, "Bragg gratings in multimode and few-mode optical fibers," *Journal of Lightwave Technology*, vol. 18, no. 2, pp. 230–235, Feb. 2000, doi: 10.1109/50.822797.

[25] M. Wang *et al.*, "Single-mode sapphire fiber Bragg grating," *Opt Express*, vol. 30, no. 9, p. 15482, Apr. 2022, doi: 10.1364/OE.446664.

[26] M. Wang *et al.*, "Optimization of Single-mode Sapphire Waveguide Bragg Gratings," *Journal of Lightwave Technology*, pp. 1–10, 2024, doi: 10.1109/JLT.2024.3396752.

[27] P. S. Salter, M. J. Woolley, S. M. Morris, M. J. Booth, and J. A. J. Fells, "Femtosecond fiber Bragg grating fabrication with adaptive optics aberration compensation," *Opt Lett*, vol. 43, no. 24, p. 5993, 2018, doi: 10.1364/ol.43.005993.

[28] S. Kawakami and S. Nishida, "Characteristics of a doubly clad optical fiber with a low-index inner cladding," *IEEE J Quantum Electron*, vol. 10, no. 12, pp. 879–887, Dec. 1974, doi: 10.1109/JQE.1974.1068118.

[29] L. Cohen, D. Marcuse, and W. Mammel, "Radiating leaky-mode losses in single-mode lightguides with depressed-index claddings," *IEEE J Quantum Electron*, vol. 18, no. 10, pp. 1467–1472, Oct. 1982, doi: 10.1109/JQE.1982.1071409.

[30] H.-D. Nguyen *et al.*, "Heuristic modelling of laser written mid-infrared LiNbO_3 stressed-cladding waveguides," *Opt Express*, vol. 24, no. 7, p. 7777, 2016, doi: 10.1364/oe.24.007777.

[31] J.-P. Bérubé, J. Lapointe, A. Dupont, M. Bernier, and R. Vallée, "Femtosecond laser inscription of depressed cladding single-mode mid-infrared waveguides in sapphire," *Opt Lett*, vol. 44, no. 1, p. 37, 2019, doi: 10.1364/ol.44.000037.

[32] T. Wang *et al.*, "Single Crystal Fibers: Diversified Functional Crystal Material," *Advanced Fiber Materials*, vol. 1, no. 3–4, pp. 163–187, Dec. 2019, doi: 10.1007/S42765-019-00020-Z.

[33] T. Wang *et al.*, "Anisotropic growth and characterizations of large length-diameter ratio sapphire fibers via laser-heated pedestal growth technique," *J Cryst Growth*, vol. 620, p. 127363, Oct. 2023, doi: 10.1016/J.JCRYSGRO.2023.127363.

[34] V. Mezentsev, I. Bennion, A. Shestakov, and A. Okhrimchuk, "Low loss depressed cladding waveguide inscribed in YAG:Nd single crystal by femtosecond laser pulses," *Optics Express, Vol. 20, Issue 4, pp. 3832-3843*, vol. 20, no. 4, pp. 3832–3843, Feb. 2012, doi: 10.1364/OE.20.003832.

[35] P. Roldan-Varona, D. Pallares-Aldeiturriaga, L. Rodriguez-Cobo, and J. M. Lopez-Higuera, "Slit Beam Shaping Technique for Femtosecond Laser Inscription of Enhanced Plane-by-Plane FBGs," *Journal of Lightwave Technology*, vol. 38, no. 16, pp. 4526–4532, Aug. 2020, doi: 10.1109/JLT.2020.2992568.

[36] D. Wortmann, J. Gottmann, N. Brandt, and H. Horn-Solle, "Micro- and nanostructures inside sapphire by fs-laser irradiation and selective etching," *Optics InfoBase Conference Papers*, vol. 16, no. 3, pp. 197–200, 2008, doi: 10.1364/oe.16.001517.

[37] F. Mumtaz *et al.*, "Thermally robust and highly stable method for splicing silica glass fiber to crystalline sapphire fiber," *Applied Optics, Vol. 62, Issue 5, pp. 1392-1398*, vol. 62, no. 5, pp. 1392–1398, Feb. 2023, doi: 10.1364/AO.479732.

[38] B. Wang *et al.*, "Femtosecond laser inscribed helical sapphire fiber Bragg gratings," *Optics Letters, Vol. 46, Issue 19, pp. 4836-4839*, vol. 46, no. 19, pp. 4836–4839, Oct. 2021, doi: 10.1364/OL.439373.

[39] S. Bayya *et al.*, "Fusion splicing of highly dissimilar YAG crystal fiber and silica fiber with reaction bonding," *Optical Materials Express, Vol. 6, Issue 8, pp. 2560-2566*, vol. 6, no. 8, pp. 2560–2566, Aug. 2016, doi: 10.1364/OME.6.002560.

[40] J. T. Jones *et al.*, "Light Propagation Considerations for Internally Clad Sapphire Optical Fiber Using the 6Li(n,α)3H Reaction," *Journal of Lightwave Technology*, vol. 40, no. 4, pp. 1181–1187, 2022, doi: 10.1109/JLT.2021.3127863.

[41] K. V. Stepanov, A. A. Zhirnov, S. G. Sazonkin, A. B. Pnev, A. N. Bobrov, and D. A. Yagodnikov, "Non-Invasive Acoustic Monitoring of Gas Turbine Units by Fiber Optic Sensors," *Sensors 2022, Vol. 22, Page 4781*, vol. 22, no. 13, p. 4781, Jun. 2022, doi: 10.3390/S22134781.

[42] M. Wang, *et al.*, "Dataset 1 Single-mode Sapphire Fiber Temperature Sensor," *IEEE Dataport,* 2024, doi: 10.21227/c3dh-ay21